Journal of Alloys and Compounds 1042 (2025) 183868

Contents lists available at ScienceDirect

Journal of Alloys and Compounds

journal homepage: www.elsevier.com/locate/jalcom

High-throughput evaluation of hardness dependence on composition and temperature in Ni–Co binary alloy systems

Mayu Asano, Toshio Osada *, Ayako Ikeda, Taichi Abe, Thomas Hoefler, Eri Nakagawa, Takahito Ohmura

Research Center for Structural Materials, National Institute for Materials Science, 1-2-1 Sengen, Tsukuba, Ibaraki 305-0047, Japan

ARTICLE INFO

Keywords:
Hardness
Nanoindentation
Diffusion couple
Ni–Co alloy
High-throughput investigation

ABSTRACT

To accelerate the design of multicomponent alloys, it is of key importance predicting required properties and identifying specific compositions from numerous element combinations. Prediction techniques, including theoretical strengthening models, numerical simulations, and machine learning approaches, offer promising avenues for accelerating alloy development. However, achieving high-precision predictions requires large experimental composition–process–structure–property (CPSP) datasets, which demand significant time and effort to acquire. This study introduces a high-throughput evaluation approach for generating composition–process–structure–high-temperature property datasets by combining diffusion couples with high-temperature nanoindentation. Applied to a Ni–Co binary alloy system containing face-centered cubic (fcc) and hexagonal close-packed (hcp) phases, this approach efficiently obtains 1144 data points, capturing the hardness across temperatures from 300 to 773 K and Co concentrations from 2 to 98 at%. These datasets facilitate data-driven analyses of empirical formulas for solid-solution strengthening. Based on a high-temperature yielding model that separates the thermal (Peierls stress) and athermal components, a prediction equation is established for the high-temperature hardness and thermal/athermal components of solid-solution strengthening in the fcc phase of Ni–Co alloys. The temperature dependence of the hardness is divided into thermal and athermal components, which is expressed as a function of the solute concentration, revealing that the thermal component is highly dependent on the Co concentration, whereas the athermal component remains nearly independent. These findings indicate that solid-solution strengthening in Ni–Co alloys is primarily governed by thermal activation within a short-range stress field across all composition ranges.

1. Introduction

A comprehensive experimental database linking composition–process–structure–property (CPSP) is required for structural material design and practical applications. In particular, understanding the solid-solution strengthening mechanism of the face-centered cubic (fcc) phase and its temperature dependence is important for developing multicomponent alloys, such as Ni-base superalloys [1] and high-entropy alloys (HEAs) [2–5], which serve as potential high-temperature structural materials. Advanced Ni-base superalloys with a γ–γ' two-phase structure incorporate multiple elements, including Co, Cr, Mo, W, Ti, Al, and Ta [1,6]. These alloying elements are designed to partition between the γ matrix (fcc) and γ' precipitates ($L1_2$-ordered structure), strengthening both phases through solid-solution strengthening [1,7]. However, experimental datasets linking composition to mechanical properties remain limited because of the vast number of possible element combinations in multicomponent alloys. Therefore, accurately predicting mechanical properties from compositions across a wide temperature range remains a significant challenge.

The most versatile commercial software for predicting strength using numerical simulations is JMatPro (Sente Software Ltd.) [8]. This software has been widely used in industries involved in the manufacture of multicomponent superalloys, providing predictions for solid solution strengthening and its temperature dependence in alloys with more than ten elements based on empirical equations. However, the accuracy of these empirical predictions depends on the number of composition–-strength datasets for binary, ternary, and multicomponent alloys in the internal database. Therefore, increasing the number of experimental datasets is essential for improving accuracy.

* Corresponding author.
E-mail address: OSADA.Toshio@nims.go.jp (T. Osada).

https://doi.org/10.1016/j.jallcom.2025.183868
Received 16 July 2025; Received in revised form 10 September 2025; Accepted 17 September 2025
Available online 18 September 2025

As theoretical based approaches, Fleischer [9] and Labusch [10] pioneered models for dilute binary alloys. The strengthening due to the solute elements $\Delta\tau^{ss}$ are simply expressed as: $\Delta\tau^{ss} = Ac^q$; where A is a coefficient related to many parameters including material properties and dislocation characteristics [9,10]; c is the concentration of solute element; q is a constant. Both models describe the interaction between dislocations and solute elements, $q = 1/2$, and $q = 2/3$ for Fleischer's [9] and Labusch's [10] models, respectively. In many types of binary alloy systems, it was reported that $q = 2/3$, rather than $q = 1/2$. Later, theoretical and empirical extensions of Labusch's model for multicomponent alloys [11,12], including medium- and high-entropy alloys (MEAs and HEAs) [13–17], and for the temperature dependence [15,18] of the contribution of solid-solution hardening to yield stress have been proposed. However, calculations for multicomponent alloys such as Ni-base superalloy with more than ten elements can be extremely resource-intensive and often unreliable or unpredictable, since these models require several parameters.

High-throughput generation of experimental datasets and data-driven analysis can be expected to improve accuracy and expand the prediction range of solid-solution strengthening. The enhanced database must lead to an update of the existing physics-based modeling and overcome the limitations of conventional experimental trial-and-error alloy design. Especially, combinatorial methods that integrate diffusion couple and nanoindentation techniques have gained significant attention as innovative approaches for the efficient acquisition of composition–mechanical property datasets [19,20]. These methods utilize unique compositional gradient samples, including multicomponent elements, to perform multipoint measurements, enabling the rapid collection of mechanical property data corresponding to various compositions [20–24]. In addition, Goto et al. [24] successfully constructed an experimental dataset linking composition and stress–strain curves for Ni–Co–Cr alloys within a broad ternary phase diagram by combining a combinatorial method and an inverse estimation approach, with approximately 168 times faster than conventional tensile testing. However, combinatorial methods only reported mechanical properties measured at room temperature [23,24]. Since Ni-base superalloys and multicomponent alloys are primarily used at high temperatures, the development of a high-throughput experimental dataset for composition-dependent high-temperature properties is crucial.

In this study, aiming to map the mechanical properties onto the equilibrium phase diagram, a high-throughput evaluation method combining high-temperature nanoindentation [25] with a composition–gradient diffusion couple is proposed using an Ni–Co binary alloy with a well-established phase diagram as a model system. This approach enables the simultaneous acquisition of both the solute concentration and temperature dependence of the hardness. Further, as a method for utilizing the obtained experimental dataset linking CPSP, an empirical equation for predicting solid-solution strengthening across the entire Ni–Co composition range and a wide temperature range is developed.

2. Experimental

A diffusion couple of Ni–Co binary alloys was prepared by stacking pure Ni (99.9 %) and Co (99.9 %) plates, which were then bonded using spark plasma sintering in vacuum at 10 MPa and 973 K for 5 min. Subsequent annealing at 1423 K for 3000 h facilitated the diffusion of Ni and Co, followed by hot isostatic pressing at 1393 K and 98 MPa for 4 h to eliminate voids. From the resulting diffusion couple, three samples with dimensions of 5 mm × 5 mm × 1 mm were cut from an initial 10 mm × 10 mm × 1 mm piece. Prior to nanoindentation experiments, the samples were mechanically polished using abrasive SiC paper and electropolished (LectroPol-5, Struers) at 40 V and 293 K. The electrolytic solution used for electropolishing consisted of 78 mL of perchloric acid, 90 mL of distilled water, 730 mL of ethanol, and 100 mL of 2-butoxyethanol (Electrolyte A2, Struers).

Nanoindentation experiments were performed using an xSol high-temperature stage (Bruker) equipped with a diamond Berkovich indenter [25]. High-temperature experiments were conducted in a reducing atmosphere of a mixed gas of 98 % Ar and 2 % H_2 to prevent surface oxidation. The loading and unloading rates were set to 1 mN/s, with a peak load of 2 mN and holding time of 10 s. Experiments were conducted at temperatures of 300, 373, 473, 573, 673, and 773 K. Note that test temperatures were sufficiently lower than the annealing temperature of 1423 K; therefore, elemental diffusion during nanoindentation can be neglected in this study. Both the sample and indenter tip were simultaneously heated at a rate of 10 K/min. Indentation measurements were performed at 1340 points, with a spacing of 25 μm between indentations in the single-phase region and 5 μm in the two-phase region. Hardness values were estimated from load-displacement curves using the method proposed by Oliver and Pharr [26].

The microstructures of the diffusion couples were examined using scanning electron microscopy (SEM; JSM-7001FD, JEOL) combined with electron backscatter diffractometry (EBSD, Oxford Instruments) at room temperature to identify crystallographic phases and orientations. Indentations were observed using SEM (Crossbeam, ZEISS). Quantitative elemental analysis of indentations was performed by point analysis using electron probe microanalysis (EPMA; EPMA-8050G, Shimadzu).

3. Results

3.1. Composition gradient and microstructural characteristics of the diffusion couple

Fig. 1 shows the microstructure and Co concentration of the sample after nanoindentation experiments conducted at 300–573 K then cooling to room temperature. Fig. 1(a) displays an image quality map of the sample surface measured using SEM-EBSD. Stacking directions of pure Ni and Co plates are horizontal in the figure. Further, the initial stacking boundary cannot be identified, since no vertical voids arrangement or gaps were observed. This implies that the preparation conditions of the diffusion couple in this study were suitable for nanoindentation tests that are affected by voids and gaps. Indentations measurements were performed in the horizontal direction across the stacking boundary at each temperature within the indented area. The indents consisting of 5 rows and 21 columns with a spacing of 25 μm were performed with high positional accuracy. The high-magnification SEM image of the indent of Ni – 8 at% Co at 573 K shows a sharp triangular indent with a size of 1.62 μm, whereas the indentation distance is 15.4 times larger than the length, confirming that measurements were performed without deformation interference between indentations. Each indent was uniquely numbered and linked to its corresponding positional information on the sample surface. By correlating the composition data measured by point analysis EPMA at the same locations as the indentation, large number of experimental compositions–high-temperature property datasets were obtained across a broad compositional and temperature range.

Fig. 1(b) presents an EMPA element mapping of the Co concentrations on the area shown in Fig. 1(a). The right side of Fig. 1(b) corresponds to the Co-rich region, while the left side corresponds to the Ni-rich region. It can be seen that the Co concentration gradually increases from left to right, while maintaining a nearly uniform concentration in the vertical direction. Meanwhile, the Co concentration exhibited a relatively steep gradient near the initial boundary of the diffusion couple.

Fig. 1(c) shows the example of line profile for Co concentration along the horizontal line in the EPMA mapping shown in Fig. 1(b). The Co concentration within the indented area showed a gentle slope, varying continuously across the range of 8–92 at%. The steepest concentration gradient appeared at around the initial boundary, and was around 0.26 at%/μm. Meanwhile, indent size tested on the steepest gradient points at the lowest and highest temperatures of 300 and 773 K were approximately 1.31 and 1.58 μm, respectively. This means that the

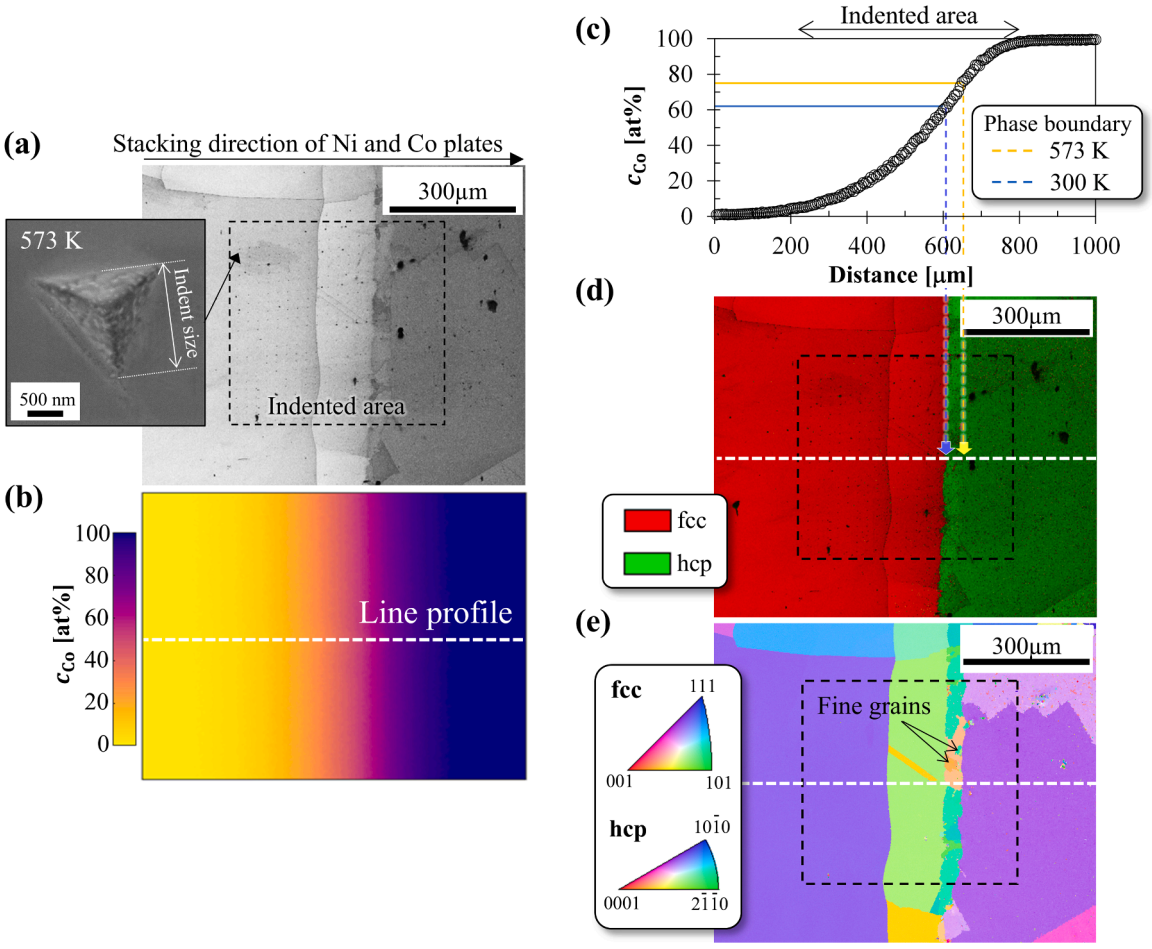

Fig. 1. Microscopy images of the Ni–Co diffusion couple sample after indentation at 300, 373, 473, and 573 K: (a) image quality map, (b) Co concentration distribution map, (c) Co concentration profile, (d) phase maps, and (e) grain orientation maps. Color lines in panels (c)–(e) indicated the presumed face-centered cubic (fcc)–hexagonal close-packed (hcp) phase boundary during high-temperature indentation.

maximum concentration difference within the indent is only 0.74 at%, since the plastic deformed zone of indentation is reported to be approximately 1.8 times larger than the indent size [27]. This confirms that the concentration gradient within the indent is small enough to be neglectable for mechanical properties. Meanwhile, the Co concentrations at phase boundary where fcc phase transforms to hcp phase were estimated to be 61 and 75 at% at 300 and 573 K, respectively, as mentioned later in 3.3. This means that the phase boundary shifts to the right by approximately 45 μm, exceeding the indentation distance of 25 μm, during heating from 300 to 573 K for nanoindentation tests. Therefore, when the indentation tests were performed at positions close to the phase boundary at each temperature, the indented phase was carefully determined.

Fig. 1(d) shows the phase map measured by SEM-EBSD. The figure shows that the fcc-hcp phase boundary nearly matches the boundary position estimated at 300 K, implying that phase boundary shifts rightward during heating and its position is nearly restored upon cooling to room temperature. However, a very small amount of fcc phase still remains within the predicted transformation region during cooling, implying that it is not completely restored to hcp phase upon cooling to room temperature, possibly due to undercooling effects.

Fig. 1(e) presents the grain orientation map obtained using SEM-EBSD. The color coding follows a standard stereographic triangle and corresponds to the orientation of the fcc and hcp phases. The presence of multiple orientations within the indentation formation area indicates that both phases were polycrystalline. The size of most grains was significantly larger than the indent size. While some fine grains, less than 45 μm in size, were observed within the region between the fcc-hcp phase boundaries estimated at 300 and 573 K, these were still much larger than the indent size. The formation of fine grains occurs due to the fcc phase transforming to hcp phase during cooling. To eliminate the influence of grain boundaries on the hardness measurements, indentations located near grain boundaries in the compositional range where no phase transformation occurred during testing, were excluded from the composition–mechanical property analysis.

3.2. Load-displacement curve

Fig. 2 shows representative load-displacement curves obtained from nanoindentation measurements. Fig. 2(a)–(d) display the curves for Ni – 3 ± 1 at% Co (Ni-3Co), Ni – 30 ± 1 at% Co (Ni-30Co), Ni – 60 ± 1 at% Co (Ni-60Co), and Ni – 97 ± 1 at% Co (Ni-97Co), respectively, which were measured at temperatures ranging from 300 to 773 K for each composition. The pop-in phenomenon, which is characteristic of the indentation deformation of crystalline materials [28], was observed in all curves during the initial stage of loading, suggesting a low initial dislocation density [29].

Following the transition from elastic to elastoplastic deformation via pop-in, the loading process followed a parabolic trajectory, which is characteristic of indentation tests using a Berkovich indenter. The curves in Fig. 2(a)–(c) correspond to the fcc phase, whereas the curve in Fig. 2 (d) represents the fcc phase at 773 K and hcp phase at other temperatures, as determined by the method described below in Fig. 3(b).

The temperature dependence of deformation for each composition

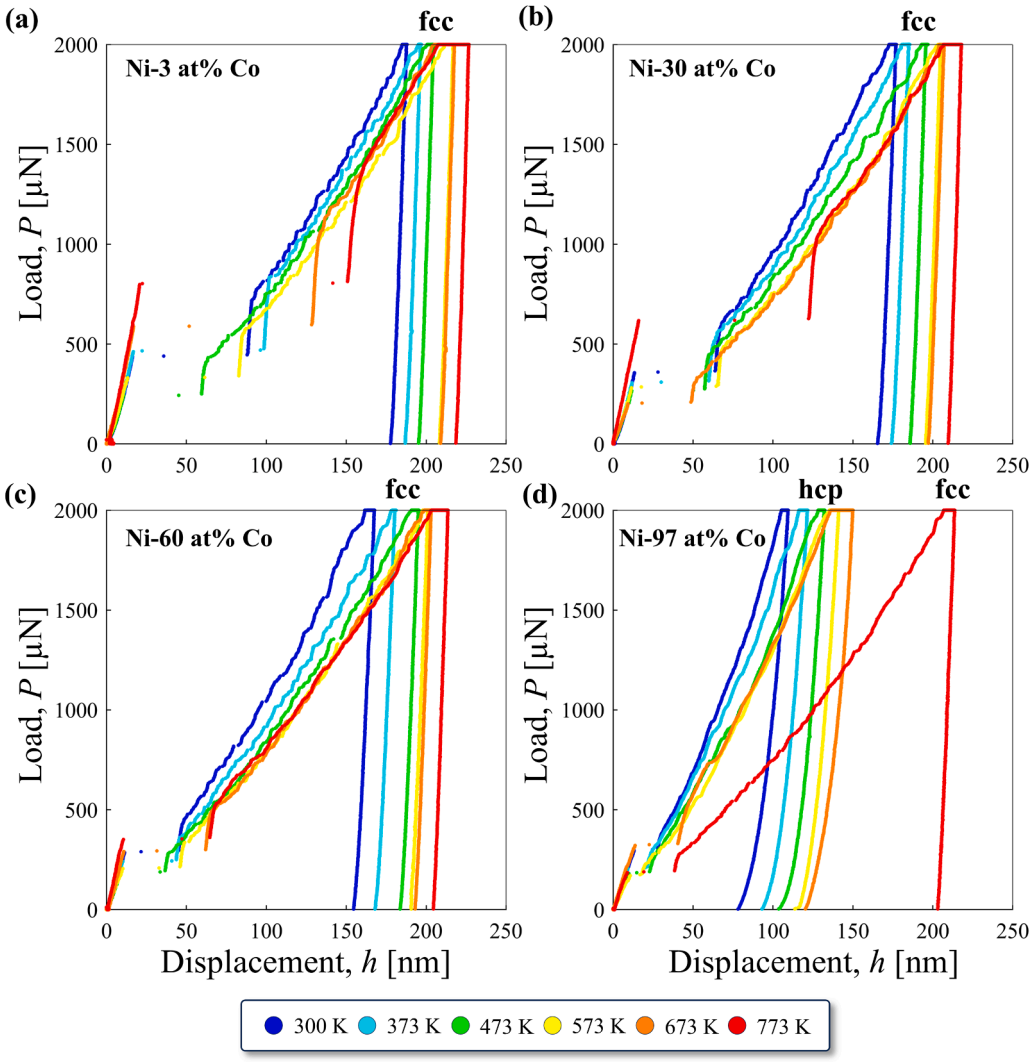

Fig. 2. Load-displacement curves at 300, 373, 473, 573, 673, and 773 K for (a) Ni-3 at% Co, (b) Ni-30 at% Co, (c) Ni-60 at% Co and (d) Ni-97 at% Co.

was as predicted, demonstrating high-temperature softening, increasing penetration depth with temperature, and greater creep displacement at the maximum holding load with increasing temperature. These results confirmed that the indentation experiments were performed with high accuracy across the entire composition and temperature ranges.

3.3. Hardness dependence on composition and temperature

Fig. 3(a) shows the relationship between the hardness and Co concentration at various temperatures. Here, solid circles and open squares represent the fcc and hcp (or hcp + fcc) phases, respectively, as determined by the phase-determination method described below.

At 773 K, where fcc is the stable phase for all compositions, the hardness exhibited a moderate increase up to approximately 80 at% Co before declining. At temperatures below 673 K, the hardness gradually increased with increasing Co concentration within the fcc phase region, with relatively small variations for each composition. In contrast, in the hcp stability region at high Co concentrations, the hardness increased sharply at approximately 70 at%, accompanied by greater variability. The hardness dependence on the Co concentration at 300 K was consistent with previous studies [24], supporting the reliability of trends observed at other temperatures.

The higher hardness of the hcp phase compared with that of the fcc phase could likely be attributed to the influence of the slip system activation during indentation deformation. Multiple slip systems had to be active during the indentation-induced deformation; however, in the hcp phase, the availability of slip systems with low critical shear stress was limited, necessitating the activation of those with higher critical shear stress. In addition, the hardness variation in the hcp phase across compositions was greater than that in the fcc phase, likely due to its anisotropic elastic behavior [24].

A phase diagram of the Ni–Co system is shown in Fig. 3(b) to determine whether each measurement point belongs to the fcc or hcp phase. Open circles and open squares represent the reported values of temperature at which the hcp phase fully transforms into the fcc phase during heating at a heating rate ranging from 2 to 10 K/min [30,31]. In this study, we defined the temperature as the "phase transformation temperature." Note that the phase transformation temperature observed during heating is slightly higher than that of the phase boundary calculated by commercial software (Thermo-Calc, Database: TCNI9) based on the CALPHAD method, which is determined as an average temperature of phase transformation temperature observed during cooling and heating [30,31]. Further, in this study, because the nanoindentation tests were performed at constant temperature on a sequence of heating up, and to consider the potential measurement errors in the reported values, we defined the upper limit of the 95 % confidence interval (CI) of experimental values as the phase boundary. The Co concentrations at the phase boundaries at 300, 373, 473, 573, and 673 K were determined to be 61, 64, 69, 75, and 82 at%, respectively. Based on the determined Co concentrations, the hardness dependence on

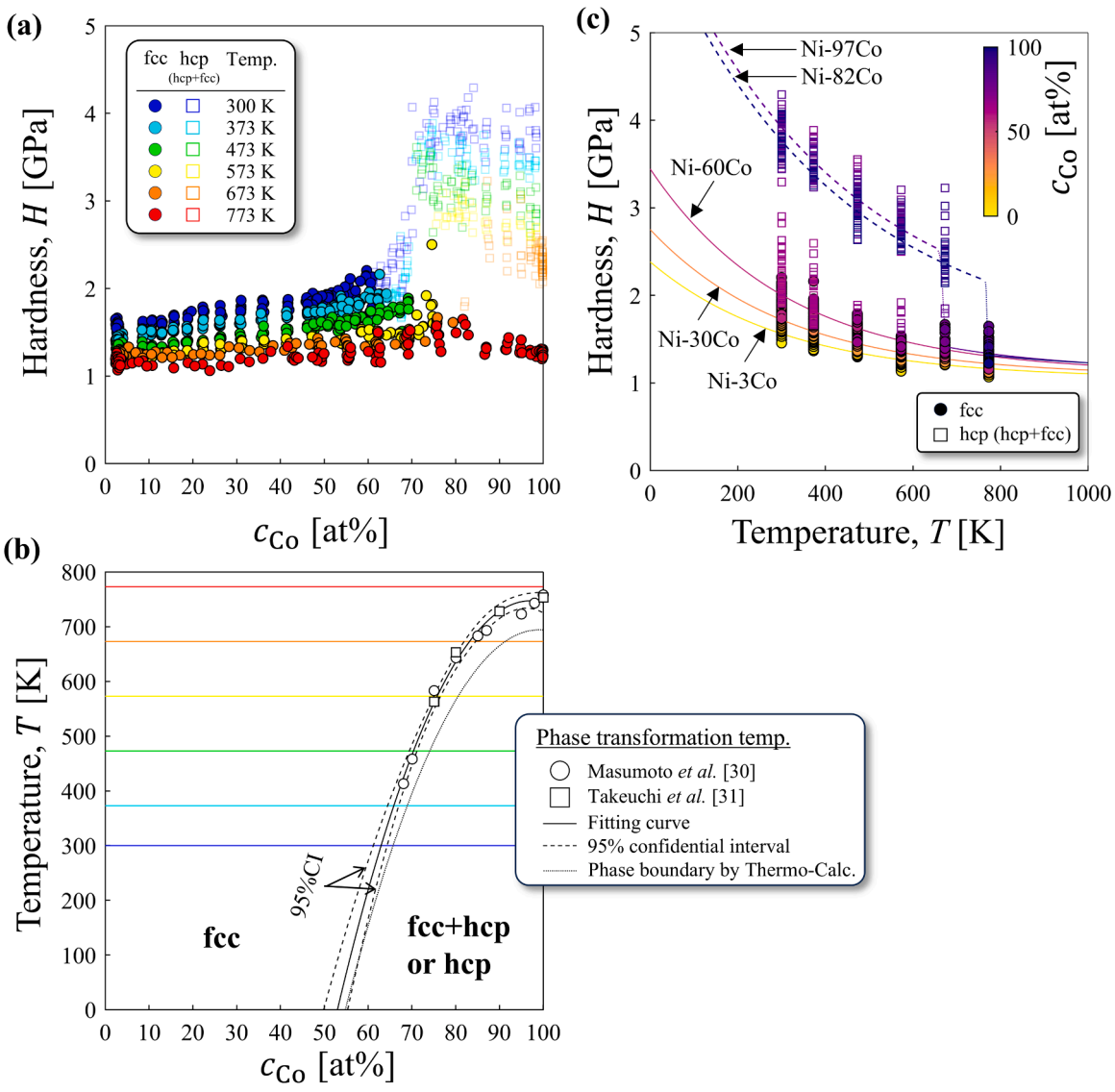

Fig. 3. (a) Hardness as a function of the Co concentration at 300, 373, 473, 573, 673, and 773 K, (b) phase diagram for Ni–Co binary alloy, and (c) hardness as a function of the temperature for different Co concentrations. Solid circles and open squares in panels (a) and (c) represent the fcc and hcp phases, respectively.

temperature and composition for the fcc phase was discussed in 4. Here, note that the data point represented by a solid yellow circle at 74.6 at% Co and 573 K in Fig. 3(a) was excluded from the fcc phase classification, as it clearly deviated from the trend observed in other fcc data points.

Consequently, a total of 764 datasets regarding composition-test temperature-hardness were obtained for the fcc phase through the proposed high-throughput evaluation method via high-temperature nanoindentation testing of diffusion couples.

Fig. 3**(c)** shows the relationship between the hardness and temperature at various Co concentrations. The solid curves show the curves obtained by fitting the data of Ni-3Co, Ni-30Co, and Ni-60Co, which are representative Co concentrations with fcc phase stable over the entire tested temperature. Meanwhile, the dashed curves show the curves obtained by fitting the data corresponding to hcp phase in Ni-82Co and Ni-97Co, which are repetitive concentrations with hcp-fcc phase transformation at high temperatures. Here, the fitting equations for the fcc phase will be discussed in 4.1.

The hardness of each composition decreased with increasing temperature before reaching a plateau, exhibiting a typical softening behavior. This trend suggested that the thermal activation of dislocation motion was the primary mechanism governing indentation-induced deformation. Furthermore, the hcp phase exhibited a distinct temperature dependence at lower temperatures under high Co concentrations. This was followed by a sudden decrease in hardness owing to the phase transformation to fcc. The temperature at which the hardness drop increased with increasing Co concentration, aligned well with the phase transformation temperature shown in Fig. 3**(b)**.

4. Discussion

4.1. Formulation of hardness dependence on temperature and composition in the fcc phase

A high-throughput evaluation approach is useful for data-driven analyses for constructing an empirical equation of solid-solution strengthening. The yield stress (σ_y) is governed by two factors related to temperature T, which act as fundamental mechanisms resisting dislocation motion [32]. The first factor involves obstacles such as the Peierls barrier, which strongly depends on the crystal structure of the material. These obstacles, typically ranging from one to several interatomic distances in size, constitute short-range resistance. They can be overcome through the thermal activation motion of dislocation driven

by thermal fluctuations, making them highly sensitive to temperature. The second factor consists of obstacles attributed to line and plane defects, such as dislocations and grain boundaries. Unlike short-range resistance, the movement required for dislocations to bypass these obstacles spans distances much larger than interatomic spacings, forming long-range resistance. The energy barrier for overcoming these obstacles is extremely high, rendering them largely unaffected by temperature.

Thus, the yield stress $\sigma_y(T)$ consists of both thermal and athermal components and can be expressed as:

$$\sigma_y(T) = \sigma_{\mathrm{th}}(T) + \sigma_{\mathrm{ath}} \tag{1}$$

where σ_{th} and σ_{ath} represent the stresses required to overcome thermal and athermal barriers, respectively.

The temperature-dependent Peierls stress σ_{p} (a thermal component) can be described as follows [18]:

$$\sigma_{\mathrm{p}}(T) = \frac{2G}{1-\nu}\exp\left(\frac{-2\pi\omega_0}{b}\right) \times \exp\left(\frac{-2\pi\omega_0}{b}\alpha T\right) \tag{2}$$

where G is the shear modulus, ν is Poisson's ratio, b is the Burgers vector, and ω_0 is the half-width of the dislocation core, which corresponds to the spacing of the glide plane divided by $1-\nu$ [33] at 0 K. The parameter α is a small positive constant, approximately $1/3T_{\mathrm{m}}$, where T_{m} is the melting point.

Furthermore, Wu et al. [18] demonstrated that the temperature-dependent part of the yield stress $\sigma_{\mathrm{th}}(T)$ is equivalent to the Peierls stress $\sigma_{\mathrm{p}}(T)$ for fcc crystals. This allowed for a simplified expression of Eq. (1) as follows:

$$\sigma_y(T) = \sigma_{\mathrm{th}}^0\exp\left(-\frac{T}{C}\right) + \sigma_{\mathrm{ath}} \tag{3}$$

where σ_{th}^0, σ_{ath}, and C are fitting parameters determined from least-squares fits to the experimental dataset, and the thermal part of σ_{th} is given by $\sigma_{\mathrm{th}}^0\exp\left(-\frac{T}{C}\right)$.

By comparing Eqs. (2) and (3), σ_{th}^0 and C can be expressed as:

$$\sigma_{\mathrm{th}}^0 = \sigma_{\mathrm{p}}(0) = \frac{2G}{1-\nu}\exp\left(\frac{-2\pi\omega_0}{b}\right) \tag{4}$$

$$C = \frac{b}{2\pi\omega_0\alpha} \tag{5}$$

Wu et al. also determined the values of σ_{th}^0, σ_{ath}, and C from the experimentally observed temperature dependence of the yield stress for polycrystalline pure Ni and Ni-50 at% Co alloys. The reported values were $\sigma_{\mathrm{th}}^0 = 46$ and 130 MPa, $\sigma_{\mathrm{ath}} = 70$ and 50 MPa, and C= 308 and 336 K [18]. The results show that σ_{th}^0 depends significantly on the Co concentration, while σ_{ath} exhibits minimal dependence. In addition, C is less affected by the Co concentration, as the variation in T_{m}, which is an important parameter for α in Eq. (5), is negligible.

A total of 764 hardness datasets, covering both the composition and high-temperature hardness obtained through the high-throughput evaluation method, are useful for realizing data-driven analyses for developing an empirical equation of solid-solution strengthening, as previously discussed. The hardness measured by nanoindentation experiments shows a strong correlation with the yield stress [24]. Therefore, in the following discussion, the hardness H is treated as σ_y in Eqs. (1) and (3).

$$H(T) = H_{\mathrm{th}}(T) + H_{\mathrm{ath}} \tag{6}$$

$$H(T) = H_{\mathrm{th}}^0\exp\left(-\frac{T}{C}\right) + H_{\mathrm{ath}} \tag{7}$$

where $H_{\mathrm{th}}(T)$ represents the thermal component of the hardness, H_{th}^0 is the thermal component of the hardness at 0 K, and H_{ath} is the athermal component of the hardness. Based on experimentally determined values for σ_{th}^0, σ_{ath}, and C [18], in this study, H_{th}^0 and H_{ath} are assumed to be parameters influenced by the Co concentration, while C is considered a Co-independent parameter.

Eq. (7) is rewritten as a function of the Co concentration (c_{Co}) by:

$$H(c_{\mathrm{Co}}, T) = \left(\Delta H_{\mathrm{th}}^{\mathrm{ss},0}(c_{\mathrm{Co}}, 0) + H_{\mathrm{th}}^{\mathrm{Ni},0}\right)\exp\left(-\frac{T}{C}\right) + \left(\Delta H_{\mathrm{ath}}^{\mathrm{ss}}(c_{\mathrm{Co}}) + H_{\mathrm{ath}}^{\mathrm{Ni}}\right) \tag{8}$$

where $\Delta H_{\mathrm{th}}^{\mathrm{ss},0}(c_{\mathrm{Co}}, 0)$ represents the hardness increment due to solid-solution strengthening at 0 K in the thermal component H_{th}^0; $H_{\mathrm{th}}^{\mathrm{Ni},0}$ is the thermal component at 0 K for the hardness of pure Ni; $\Delta H_{\mathrm{ath}}^{\mathrm{ss}}(c_{\mathrm{Co}})$ is the hardness increment due to solid-solution strengthening in the athermal component H_{ath}; and H_{ath}^{Ni} is the athermal component for the hardness of pure Ni. Meanwhile, Eq. (6) for pure Ni is expressed as:

$$H(T) = H_{\mathrm{th}}^{\mathrm{Ni},0}\exp\left(-\frac{T}{C}\right) + H_{\mathrm{ath}}^{\mathrm{Ni}} \tag{9}$$

The temperature dependence of the hardness for 2–3 at% Co, which is the lowest Co concentration in experimental datasets, is almost identical to that of pure Ni. Therefore, assuming C = 308 K [18], which has been reported as a result of tensile tests of pure Ni at 77–673 K, as an initial value for fitting, $H_{\mathrm{th}}^{\mathrm{Ni},0}$ and $H_{\mathrm{ath}}^{\mathrm{Ni}}$ are determined to be 1.34 and 1.05 GPa, respectively.

Parameters other than $H_{\mathrm{th}}^{\mathrm{Ni},0}$ and $H_{\mathrm{ath}}^{\mathrm{Ni}}$ were subsequently determined by multivariate least-squares fitting using all measurement points for the fcc phase as shown in 3.3. Here, the concentration-dependent terms $\Delta H_{\mathrm{th}}^{\mathrm{ss},0}(c_{\mathrm{Co}}, 0)$ and $\Delta H_{\mathrm{ath}}^{\mathrm{ss}}(c_{\mathrm{Co}})$ were defined as follows:

$$H(c_{\mathrm{Co}}, T) = \left(\sum_{i=1}^{m} P_i {c_{\mathrm{Co}}}^{m+1-i} + H_{\mathrm{th}}^{\mathrm{Ni},0}\right)\exp\left(-\frac{T}{C}\right) + \left(\sum_{j=1}^{n} K_j {c_{\mathrm{Co}}}^{n+1-j} + H_{\mathrm{ath}}^{\mathrm{Ni}}\right) \tag{10}$$

where m and n are the polynomial degrees. As shown in Fig. 3**(c)**, hardness for fcc phase over the entire composition range converges to a constant value at high temperatures above 773 K. This implies that the effect of Co composition on athermal components is presumably small. Thus, the term of $\sum_{j=1}^{n} K_j {c_{\mathrm{Co}}}^{n+1-j}$ in athermal component was simply defined as a linear function ($n = 1$) to avoid overfitting by using n > 1. The determination $n = 1$ seems to be physically reasonable, since the atomic size effect varies linearly on athermal component. Meanwhile, the term of $\sum_{i=1}^{m} P_i {C_{\mathrm{Co}}}^{m+1-i}$ in thermal component was determined as a cubic function ($m = 3$), because R^2 value showed the highest value at m = 3, when the hardness were fitted with a simple function varying from m = 1–3. The nonlinearity of hardness depending on Co concentration is also reasonable from the result that hardness of the fcc phase at 773 K showed slightly increased with increasing Co up to approximately 80 % and decreased to the hardness of Co above 80 %.

By multivariate least-squares fitting 764 datasets of the fcc structure regarding composition (c_{Co}) -test temperature (T) -hardness (H) with Eq. (10) (m = 3 and n = 1), all the parameters can be determined. Thus, Eq. (10) can be conclusively described as:

$$H(c_{\mathrm{Co}}, T) = \left(-6.44\times10^{-6}{c_{\mathrm{Co}}}^3 + 7.63\times10^{-4}{c_{\mathrm{Co}}}^2 - 6.04\times10^{-3}c_{\mathrm{Co}} + 1.34\right)\exp\left(-\frac{T}{314}\right) + \left(1.03\times10^{-3}c_{\mathrm{Co}} + 1.05\right) \tag{11}$$

Here, the coefficient of determination of the equation shows R^2 = 0.9051, which was a very high value. Therefore, by using this formula, it is possible to predict the temperature and Co composition dependence of hardness of fcc phase with high accuracy. All determined parameters are listed in Table 1.

Fig. 4(a) shows the surface fit obtained using Eq. (11), along with the

Table 1
Summary of parameters determined from datasets in this study.

Thermal components, H_{th}					Athermal components, H_{ath}	
Thermal components at 0 K, H^0_{th}				C		
$\Delta H^{ss,0}_{th}(c_{Co},0)$ #			$H^{Ni,0}_{th}$ #		$\Delta H^{ss}_{ath}(c_{Co})$ #	H^{Ni}_{ath} #
P_1[GPa/at%^{3}]	P_2 [GPa/at%^{2}]	P_3 [GPa/at%]	[GPa]	[K]	K_1 [GPa/at%]	[GPa]
-6.44×10^{-6}	7.63×10^{-4}	-6.04×10^{-3}	1.34	314	1.03×10^{-3}	1.05

$\Delta H^{ss,0}_{th}(c_{Co},0)$ is the hardness increment due to solid-solution strengthening at 0 K; $H^{Ni,0}_{th}$ is the thermal component at 0 K for the hardness of pure Ni; $\Delta H^{ss}_{ath}(c_{Co})$ is the hardness increment due to solid-solution strengthening in the athermal component H_{ath}; H^{Ni}_{ath} is the athermal component of the hardness of pure Ni.

measurement points. Most measurement points align well with the curved surface, indicating that the surface fit achieved high accuracy. This accuracy was attributed to the extensive dataset obtained from high-throughput nanoindentation experiments. Therefore, the prediction equation Eq. (11) for hardness is highly valuable for designing multicomponent systems at high temperatures. In particular, the reliability of the prediction equations is high within the composition and temperature ranges where the experimental values are distributed, and these ranges are sufficiently broad to establish a comprehensive database.

The three-dimensional hardness map in Fig. 4(a) reveals valuable insights from different perspectives. Fig. 4(b), projected onto the $T - c_{Co}$ plane, visualizes the relationship between hardness, composition, and temperature within the phase diagram of the Ni–Co system. Fig. 4(c),

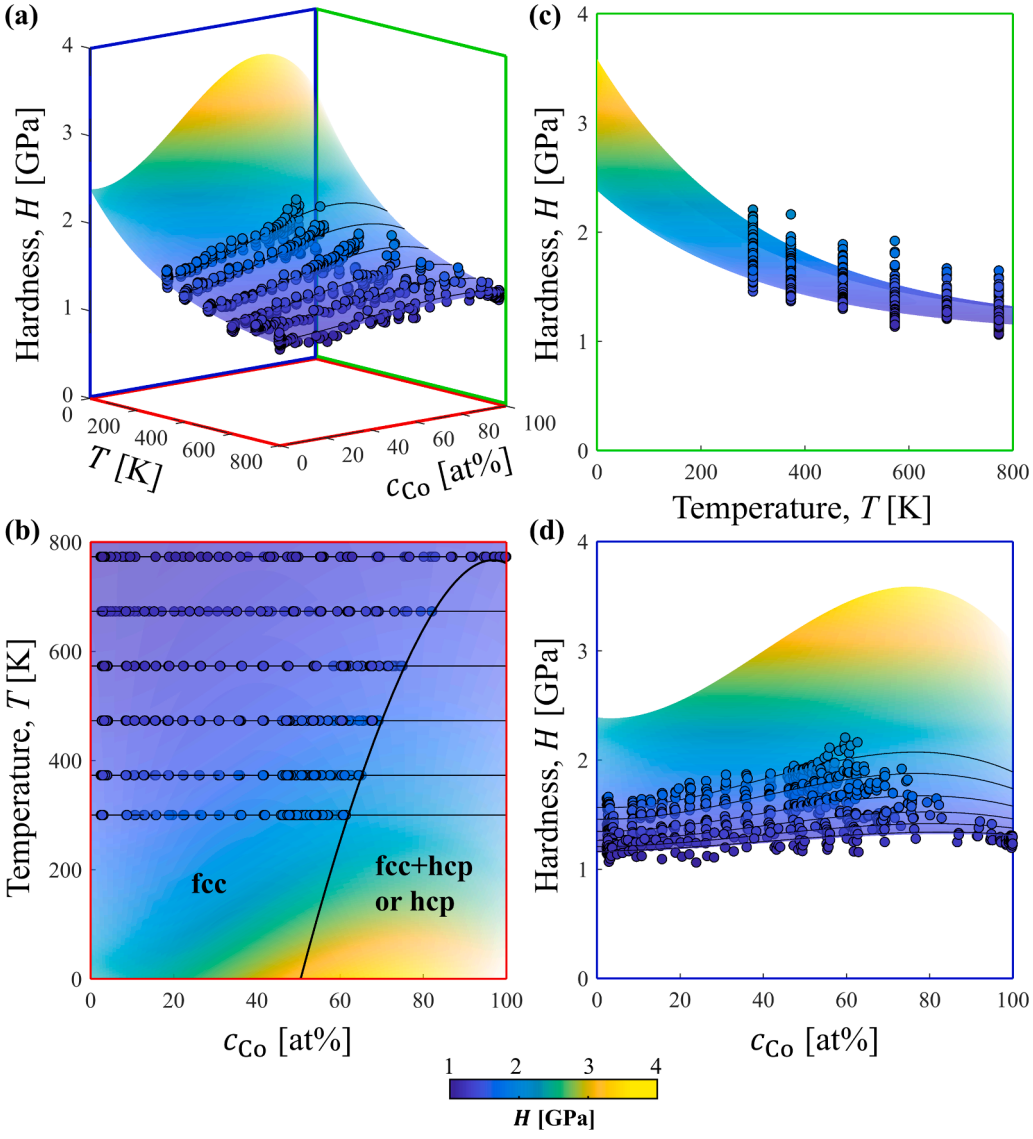

Fig. 4. (a) Relationship among Co concentration, temperature, and hardness; (b) temperature as a function of the Co concentration; (c) hardness as a function of temperature; and (d) hardness as a function of the Co concentration.

projected onto the $H-T$ plane, illustrates the temperature dependence of hardness for each composition, demonstrating a softening behavior with increasing temperature owing to the thermally activated motion of dislocations. Fig. 4(d), projected onto the $H-c_{\mathrm{Co}}$ plane, presents the composition dependence of the hardness at various temperatures. The effect of solute element addition across a wide range of compositions and temperatures was analyzed in comparison with previous studies [21–24], which primarily focused on solid-solution strengthening at room temperature. The results revealed that solid-solution strengthening occurred with varying degrees of influence depending on the temperature. As shown in Fig. 4(a) and (d), the strengthening effect was more pronounced at lower temperatures. The dependence of the hardness on the Co concentration is discussed in 4.2, with particular focus on the predicted results at 0 K, where the solid-solution strengthening effect is most significant.

Further, this study focused only on solid solution strengthening in the fcc phase. Because crystal orientation has a large effect on the hardness of the hcp phase [24], it was difficult to discuss the dependence of the hardness of the hcp phase solely on composition and temperature. However, the high-throughput evaluation method will also contribute to the construction of a strengthening model for the hcp phase in the future.

4.2. Thermal and athermal components of solid-solution strengthening

A data-driven analysis of high-throughput generated datasets provides a clear understanding of the contributions of the thermal ($\Delta H_{\mathrm{th}}^{\mathrm{ss},0}(c_{\mathrm{Co}},0)$, $H_{\mathrm{th}}^{\mathrm{Ni},0}$, and $\exp\left(-\frac{T}{C}\right)$) and athermal ($\Delta H_{\mathrm{ath}}^{\mathrm{ss}}(c_{\mathrm{Co}})$ and $H_{\mathrm{ath}}^{\mathrm{Ni}}$) components to the hardness at high temperatures ($H(c_{\mathrm{Co}},T)$). Notably, this approach enables the separation of the influence of solute elements on the hardness into thermal and athermal components, as expressed in Eq. (11).

Fig. 5(a) presents the H and H_{ath}, calculated from Eq. (11), as a function of the Co concentration. The solid lines in different colors represent the total hardness $H(T)$, which is the sum of both components, while the purple dashed line indicates the athermal component H_{ath}, as defined in Eq. (6). In addition to the experimental results obtained from 300 to 773 K, the extrapolated values of H at 0 and 1768 K, corresponding to the melting point of Co [34], are also shown. The difference between the $H(T)$ and H_{ath} corresponds to the thermal component $H_{\mathrm{th}}(T)$ in Eq. (6). As shown in Fig. 5(a) the $H_{\mathrm{th}}(0\ \mathrm{K})$ is significantly higher than the temperature-independent H_{ath}, indicating the difficulty in overcoming the Peierls barrier without thermal assistance. Meanwhile, the $H(T)$ decreased significantly with increasing temperature due to the

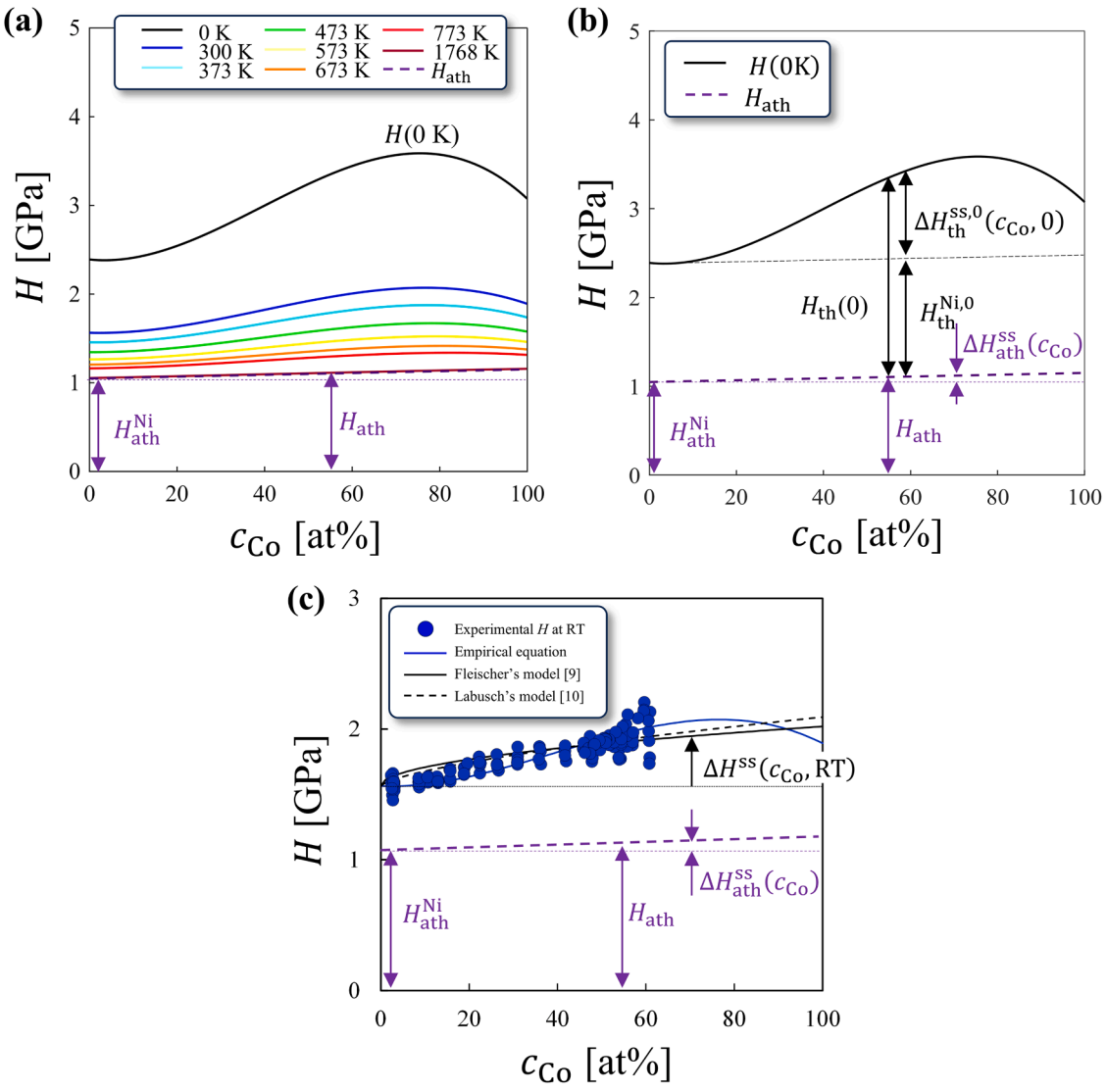

Fig. 5. The hardness (H) and its thermal component (H_{ath}) calculated by Eq. (11) as a function of the Co concentration (a) H at experimental temperature, extrapolated H at 0 and 1768 K (melting point of Co) and H_{ath}, (b) extrapolated H and H_{ath} at 0 K, and (c) the comparison of estimated hardness at RT.

reduction in the temperature-dependent $H_{th}(T)$, suggesting that dislocation motion was thermally activated to overcome the barrier. In addition, the $H(T)$ increased with increasing Co concentration, reaching a peak at approximately 80 at% Co. This peak arose from the interplay between the thermal and athermal components of Co solid-solution strengthening.

For a more detailed discussion, the $H(0\ \mathrm{K})$, which exhibits significant solid-solution strengthening, was selected along with the H_{ath}, as shown in Fig. 5(b). It should be noted that Fig. 5(b) represents a scenario in which the fcc phase is assumed to be stable at 0 K, whereas the hcp phase becomes stable at higher Co concentrations, as indicated in Fig. 3(b). Compared with H_{ath}^{Ni} for pure Ni, the H_{ath} increased slightly with increasing Co concentration. The increment of the H_{ath} due to solid-solution strengthening, ΔH_{ath}^{ss}, is expressed as:

$$\Delta H_{ath}^{ss}(c_{Co}) = 1.03 \times 10^{-3} c_{Co} \tag{12}$$

Meanwhile, compared with $H_{th}(0\ \mathrm{K})$ for pure Ni (the sum of the $H_{th}^{Ni,0}$ and H_{ath}^{Ni}), the $H(0\ \mathrm{K})$ exhibits a significant increase with increasing Co concentration, peaking at approximately 80 at% Co. The increment in $H(0\ \mathrm{K})$ due to solid-solution strengthening, $\Delta H_{th}^{ss,0}$, can be expressed as:

$$\Delta H_{th}^{ss,0}(c_{Co}, 0) = -6.44\times10^{-6} {c_{Co}}^3 + 7.63 \times 10^{-4} {c_{Co}}^2 - 6.04\times10^{-3} c_{Co} \tag{13}$$

As shown in Fig. 5(b), the contribution of thermal components to solid-solution strengthening by solute atoms was significantly greater than that of athermal components. In other words, the $\Delta H_{th}^{ss,0}(c_{Co}, 0)$ was highly dependent on the Co concentration of the solute, whereas the $\Delta H_{ath}^{ss}(c_{Co})$ remained nearly independent of the Co concentration. Therefore, the peak value of the $H(T)$ occurred at approximately 80 at% Co, aligning with the maximum of $\Delta H_{th}^{ss,0}(c_{Co}, 0)$.

These results suggested that thermal activation was the dominant solid-solution strengthening mechanism for Ni–Co across all composition ranges. As discussed in the previous section, the thermal component was primarily governed by short-range resistance, with individual Co atoms contributing to this effect. This mechanism remained relevant even at higher Co concentrations. The peak of the ΔH_{th}^{ss} appearing at a Co concentration higher than 50 at% was attributed to changes in the dislocation core structure, resulting from a decrease in the stacking fault energy as the Co concentration increased.

Notably, the maximum value of the ΔH_{th}^{ss} was comparable to the H_{th} of pure Ni, which represented the intrinsic resistance of Ni. Previous studies have suggested minimal solid-solution strengthening above RT with Co addition to Ni compared to Ta, Mo, Pt, Fe, or Cr addition to Ni [21,23,24]. As shown in Fig. 5(a), the present hardness results at RT confirm the weak contribution of Co to hardness, similar to previous studies [23,24]. On the other hand, the present results indicate that this may not hold true at low temperatures below RT. Further experimental validation at low temperatures is necessary to clarify this point.

Further, compared with Fleischer's [9] and Labusch's [10] models, the proposed data-driven empirical equation has several advantages. As an example, a comparison of estimated hardness at RT is shown in Fig. 5 **(c)**. Here, the prediction lines by Fleischer's model and Labusch's model are obtained by determining constants K_1 and K_2, assuming that hardness increases at RT due to Co addition, $\Delta H^{ss}(c_{Co})$, follows $\Delta H^{ss}(c_{Co}) = K_1 {c_{Co}}^{1/2}$, and $\Delta H^{ss}(c_{Co}) = K_2 {c_{Co}}^{2/3}$, respectively, as mentioned in the introduction. Here, it was determined that $K_1 = 4.56 \times 10^{-2}$ and $K_2 = 2.45 \times 10^{-2}$.

As shown in the figure, the present empirical equation showed a similar tendency of c_{Co} dependence below 60 at% Co to Fleischer's and Labusch's model. On the other hand, above 60 at% Co, the two theoretical models showed a monotonically increasing hardness, whereas the empirical equation in this study was able to describe the clear peak in hardness that appeared in the experiment at 773 K. Furthermore, a key advantage of data-driven analysis by using high-throughput datasets is that it allows us to discuss both the c_{Co} contributions to thermal and athermal components of solid solution strengthening simultaneously. As a result, by subtracting Eq. (9) from Eq. (11) the $\Delta H^{ss}(c_{Co}, T)$ can be expressed as follows:

$$\Delta H^{ss}(c_{Co}, T) = \Delta H_{th}^{ss}(c_{Co}, T) + \Delta H_{ath}^{ss}(c_{Co})$$

$$= \left(-6.44\times10^{-6} {c_{Co}}^3 + 7.63 \times 10^{-4} {c_{Co}}^2 - 6.04\times10^{-3} c_{Co}\right) \exp\left(-\frac{T}{314}\right) + 1.03 \times 10^{-3} c_{Co} \tag{14}$$

By organizing the temperature dependence of only the thermal component, as shown in the first term of Eq. 14, it becomes possible to derive an empirical equation for the temperature dependence of solid solution strengthening, which was difficult to achieve with other models. Furthermore, the nanoindentation method allows for the acquisition of large datasets of composition-hardness relation eliminating the grain boundary strengthening, which is difficult to obtain using conventional evaluation methods [18] such as casting, forging, and high-temperature tensile testing. Thus, the other advantage of this method is that it enables accurate and rapid evaluation of solid solution strengthening without being affected by grain boundaries.

4.3. Comparison of predicted and experimental results

Fig. 6 compares the experimental and predicted values to validate the formulation of Eq. (11). Meanwhile, the solid and dashed lines represent the upper and lower limits of the 95 % prediction intervals (PI)

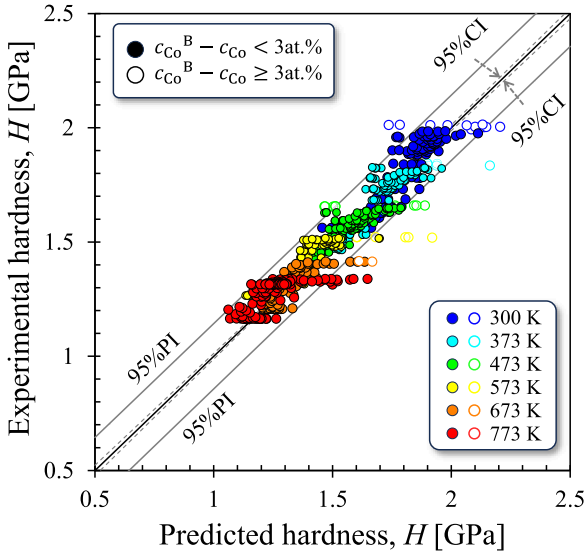

Fig. 6. Comparison of experimental and predicted hardness based on Eq. (11) with compositions from 2 to 98 at% Co at 300, 373, 473, 573, 673, and 773 K.

and 95 % confidence intervals (CI), respectively. Additionally, hardness data for composition with a concentration difference of less than 3 % from the phase boundary composition (c_{Co}^{B}) are marked with open circles.

It can be seen that the Co composition and test temperature dependence on high-temperature hardness is well expressed by Eq. (11), because of high R^2 values ($R^2 = 0.9051$) and narrow 95 % CI. Especially, at all tested temperatures except 673 and 773 K, the predicted values with a concentration difference of 3 % or more from the phase boundary composition are in good agreement with experimental values and within 95 % PI. Meanwhile, some data where the concentration difference from c_{Co}^{B} was less than 3 % are outside of 95 % PI, implying the accuracy of prediction slightly decreased. The decrease in prediction accuracy near c_{Co}^{B} may be due to the transition of deformation mechanisms. It has been reported that the stacking fault energy in fcc single-phase Ni–Co systems decreases linearly with increasing solute concentration up to the phase boundary [35,36]. A low stacking fault energy led to dissociation of dislocations, which promoted the formation of stacking faults and deformation twins during indentation close to the phase boundaries.

Another factor to consider was the unavoidable decrease in accuracy owing to the increased difficulty of nanoindentation experiments at elevated temperatures. This was evident from the large difference between the experimental and predicted values at 673 and 773 K, although all the data belong to the fcc single phase (Fig. 3(a)). However, the relatively large difference observed between 60 and 90 at% Co suggested that the accuracy of the load-displacement curve values was not solely dependent on the measured sample temperature. For example, the actual sample temperature may have been slightly lower than the target value, preventing the system from reaching the temperature range where single-phase fcc was stable and instead placing it within the fcc+hcp phase region. Furthermore, the accuracy of the phase diagram shown in Fig. 3(b) should be verified in future works.

For enhancing the accuracy of hardness predictions and further discussing the solid solution strengthening mechanism, it will be necessary to conduct indentation experiments at temperatures lower than 300 K and analyze the deformation mechanism at higher Co concentrations in greater detail. Further, ensuring the stability of high-temperature indentation experiments will be also particularly important for the high-temperature applications of Ni-base superalloys.

5. Conclusions

A high-throughput method for acquiring composition–high-temperature datasets was developed using Ni–Co binary alloys with temperatures ranging from 300 to 773 K and compositions from 2 to 98 at% Co to investigate the composition and temperature dependence of hardness. A prediction equation for solid-solution strengthening in the fcc phase of Ni–Co was proposed based on a comprehensive dataset. A total of 1144 data points for hardness, composition, and temperature were acquired using a high-throughput evaluation method that combined a diffusion couple with high-temperature nanoindentation. The hardness increased with the Co concentration up to the phase-transformation point at 300–673 K, while at 773 K, it increased to approximately 80 at% before decreasing within the single fcc phase. The temperature dependence of the hardness decreased with increasing temperature and then plateaued for all compositions owing to the thermal activation motion of dislocations, with the fcc–hcp phase transformation temperature shifting higher with increasing Co concentration. Using 764 data points for the fcc phase, a prediction equation for solid-solution strengthening as a function of temperature and composition was successfully formulated, decomposing the strengthening into thermal and athermal components through highly accurate surface fitting. The composition dependence of the hardness at 0 K was evaluated separately for these components, revealing that the thermal component was highly dependent on the Co concentration, whereas the athermal component remained nearly unaffected. These findings suggested that solid-solution strengthening by Co addition was primarily governed by thermal activation processes in a short-range stress field. This method can be applied to other alloy systems as well, and it also allows for automated evaluation by using our newly developed system [37]. By expanding the high-throughput dataset of various multi-component alloys [20] and developing empirical formulas for solid-solution strengthening, which accelerates the design of high-performance multicomponent alloys.

Authors' declaration

The authors have a patent pending for NIMS related to the method presented in this study.

CRediT authorship contribution statement

Mayu Asano: Methodology, Investigation, Data Curation, Writing – Original Draft. **Toshio Osada:** Conceptualization, Writing – Review and Editing, Project Administration, Supervision. **Ayako Ikeda:** Methodology, Investigation, Data Curation. **Taichi Abe:** Methodology, Data Curation. **Thomas Hoefler:** Data Curation, Formal Analysis. **Eri Nakagawa:** Investigation. **Takahito Ohmura:** Conceptualization, Resources, Writing – Review and Editing, Supervision, Project Administration, Funding Acquisition.

Declaration of Competing Interest

The authors declare that they have no known competing financial interests or personal relationships that could have appeared to influence the work reported in this paper.

Acknowledgements

This study was supported by the Innovative Science and Technology Initiative for Security (JPJ004596) promoted by Acquisition, Technology & Logistics Agency (ATLA), Japan. The authors extend their gratitude to Ms. Chieko Toku for assisting with sample preparation. We would like to thank Editage (www.editage.com) for English language editing.

References

[1] R.C. ReedThe Superalloys: Fundamentals and Applications. Cambridge University Press, Cambridge. 1017/cbo9780511541285.200610.
[2] B. Cantor, I.T.H. Chang, P. Knight, A.J.B. Vincent, Microstructural development in equiatomic multicomponent alloys, Mater. Sci. Eng. A 375–377 (2004) 213–218, https://doi.org/10.1016/j.msea.2003.10.257.
[3] J.-W. Yeh, S.-K. Chen, S.-J. Lin, J.-Y. Gan, T.-S. Chin, T.-T. Shun, C.-H. Tsau, S.-Y. Chang, Nanostructured high-entropy alloys with multiple principal elements: novel alloy design concepts and outcomes, Adv. Eng. Mater. 6 (2004) 299–303, https://doi.org/10.1002/adem.200300567.
[4] D.B. Miracle, O.N. Senkov, A critical review of high entropy alloys and related concepts, Acta Mater. 122 (2017) 448–511, https://doi.org/10.1016/j.actamat.2016.08.081.
[5] E.P. George, W.A. Curtin, C.C. Tasan, High entropy alloys: a focused review of mechanical properties and deformation mechanisms, Acta Mater. 188 (2020) 435–474, https://doi.org/10.1016/j.actamat.2019.12.015.
[6] L. Wu, T. Osada, T. Yokokawa, Y. Chang, K. Kawagishi, The temperature dependence of strengthening mechanisms in Ni-based superalloys: a newly redefined cuboidal model and its implications for strength design, J. Alloy. Compd. 931 (2023) 167508, https://doi.org/10.1016/j.jallcom.2022.167508.
[7] T. Osada, Y. Gu, N. Nagashima, Y. Yuan, T. Yokokawa, H. Harada, Optimum microstructure combination for maximizing tensile strength in a polycrystalline superalloy with a two-phase structure, Acta Mater. 61 (2013) 1820–1829, https://doi.org/10.1016/j.actamat.2012.12.004.
[8] N. Saunders, U.K.Z. Guo, X. Li, A.P. Miodownik, J.-Ph Schillé, Using JMatPro to model materials properties and behavior, JOM 55 (2003) 60–65, https://doi.org/10.1007/s11837-003-0013-2.
[9] R.L. Fleischer, Substitutional solution hardening, Acta Met. 11 (1963) 203–209, https://doi.org/10.1016/0001-6160(63)90213-X.
[10] R. Labusch, A statistical theory of solid solution hardening, Phys. Status Solidi (b) 41 (1970) 659–669, https://doi.org/10.1002/pssb.19700410221.

[11] L.A. Gypen, A. Deruyttere, Multi-component solid solution hardening proposed model, J. Mater. Sci. 12 (1977) 1028–1033, https://doi.org/10.1007/BF00540987.
[12] L.A. Gypen, A. Deruyttere, Multi-component solid solution hardening agreement with experimental results, J. Mater. Sci. 12 (1977) 1034–1038, https://doi.org/10.1007/BF00540988.
[13] I. Toda-Caraballo, P.E.J. Rivera-Diaz-del-Castillo, Modeling solid solution hardening in high entropy alloys, Acta Mater. 85 (2015) 14–23, https://doi.org/10.1016/j.actamat.2014.11.014.
[14] I. Toda-Caraballo, A general formulation for solid solution hardening effect in multicomponent alloys, Scr. Mater. 127 (2017) 113–117, https://doi.org/10.1016/j.scriptamat.2016.09.009.
[15] C. Varvenne, A. Luque, W.A. Curtin, Theory of strengthening in fcc high entropy alloys, Acta Mater. 118 (2016) 164–176, https://doi.org/10.1016/j.actamat.2016.07.040.
[16] N.L. Okamoto, K. Yuge, K. Tanaka, H. Inui, E.P. George, Atomic displacement in the CrMnFeCoNi high-entropy alloy – a scaling factor to predict solid solution strengthening, AIP Adv. 6 (2016) 125008, https://doi.org/10.1063/1.4971371.
[17] L. Li, Z. Chen, S. Tei, Y. Matsuo, R. Chiba, K. Yuge, H. Inui, E.P. George, Analysis of the temperature-dependent plastic deformation of single crystals of quinary, quaternary and ternary equiatomic high- and medium-entropy alloys of the Cr-Mn-Fe-Co-Ni system, Sci. Technol. Adv. Mater. 25 (2024) 2376524, https://doi.org/10.1080/14686996.2024.2376524.
[18] Z. Wu, H. Bei, G.M. Pharr, E.P. George, Temperature dependence of the mechanical properties of equiatomic solid solution alloys with face-centered cubic crystal structures, Acta Mater. 81 (2014) 428–441, https://doi.org/10.1016/j.actamat.2014.08.026.
[19] J.-C. Zhao, A combinatorial approach for efficient mapping of phase diagrams and properties, J. Mater. Res. 16 (2001) 1565–1578, https://doi.org/10.1557/JMR.2001.0218.
[20] A. Ikeda, K. Goto, T. Osada, I. Watanabe, K. Kawagishi, High-throughput mapping method for mechanical properties, oxidation resistance, and phase stability in Ni-based superalloys using composition-graded unidirectional solidified alloys, Scr. Mater. 193 (2021) 91–96, https://doi.org/10.1016/j.scriptamat.2020.10.043.
[21] O. Franke, K. Durst, M. Göken, Nanoindentation investigations to study solid solution hardening in Ni-based diffusion couples, J. Mater. Res. 24 (2009) 1127–1134, https://doi.org/10.1557/jmr.2009.0135.
[22] L. Haußmann, S. Neumeier, A. Hausmann, E. Bergamaschi, M. Göken, Combinatorial materials research for the development of new advanced CoNi-base superalloys, Superalloys (2024) 85–94, https://doi.org/10.1007/978-3-031-63937-1_8.
[23] S.B. Kadambi, V.D. Divya, U. Ramamurty, Evaluation of solid-solution hardening in several binary alloy system using diffusion couples combined with nanoindentation, Metall. Mater. Trans. A. 48 (2017) 4574–4582, https://doi.org/10.1007/s11661-017-4250-3.
[24] K. Goto, A. Ikeda, T. Osada, I. Watanabe, K. Kawagishi, T. Ohmura, High-throughput evaluation of stress-strain relationships in Ni-Co-Cr ternary systems via indentation testing of diffusion couples, J. Alloy. Compd. 910 (2022) 164868, https://doi.org/10.1016/j.jallcom.2022.164868.
[25] J. Ruzic, K. Goto, I. Watanabe, T. Osada, L. Wu, T. Ohmura, Temperature-dependent deformation behavior of γ and γ'single-phase nickel-based superalloys, Mater. Sci. Eng. A 818 (2021) 141439, https://doi.org/10.1016/j.msea.2021.141439.
[26] W.C. Oliver, G.M. Pharr, An improved technique for determining hardness and elastic modulus using load and displacement sensing indentation experiments, J. Mater. Res. 7 (1992) 1564–1583, https://doi.org/10.1557/JMR.1992.1564.
[27] Y. Murakami, M. Itokazu, Elastic-plastic analysis of a triangular pyramidal indentation, Int. J. Solids Struct. 34 (1997) 4005–4018, https://doi.org/10.1016/S0020-7683(97)00001-2.
[28] T. Ohmura, M. Wakeda, Pop-In phenomenon as a fundamental plasticity probed by nanoindentation technique, Materials 14 (2021) 1879, https://doi.org/10.3390/ma14081879.
[29] K. Sekido, T. Ohmura, T. Hara, K. Tsuzaki, Effect of dislocation density on the initiation of plastic deformation on Fe–C steels, Mater. Trans. 53 (2012) 907–912, https://doi.org/10.2320/matertrans.M2011356.
[30] H. Masumoto, Kinzoku no Kenkyu 2 (1925) 1023–1038.
[31] S. Takeuchi, T. Honma, Studies on the β-ε transformation in cobalt-nickel alloys. I: propagation process of the transformation, Sci. Rep. Res. Inst. Tohoku Univ. A 49 (1957) 492–507.
[32] A.S. Argon, Strengthening Mechanism in Crystal Plasticity, Oxford University Press, Oxford, 2008.
[33] G.E. Dieter, Mechanical Metallurgy, second ed., International Student ed., 1976, pp. 105–149.
[34] M. Hasen, K. Anderko, Constitution of binary alloys, McGraw-Hill Company, Inc, New York Toronto London, 1958, pp. 485–487.
[35] C.K.L. Davies, V. Sagar, R.N. Stevens, The effect of stacking fault energy on the plastic deformation of polycrystalline Ni-Co alloys, Acta Met. 21 (1973) 1343–1352, https://doi.org/10.1016/0001-6160(73)90084-9.
[36] L. Deléhouzée, A. Deruyttere, The stacking fault density in solid solutions based on copper, silver, nickel, aluminium and lead, Acta Met. 15 (1967) 727–734, https://doi.org/10.1016/0001-6160(67)90353-7.
[37] T. Hoefler, A. Ikeda, T. Osada, T. Hara, K. Kawagishi, T. Ohmura, Automated system for high-throughput process-structure-property dataset generation of structural materials: a γ/γ' superalloy case study, Mater. Des. 256 (2025) 114279, https://doi.org/10.1016/j.matdes.2025.114279.